Notice

This manuscript is submitted to EarthArXiv as a pre-print and has not yet been peer-reviewed. Please note that following peer-review, subsequent versions of this paper may have slightly different content. If accepted for publication, the final version of this pre-print will also be made available. Please feel free to contact the corresponding author directly. We welcome constructive feedback.

Title: Segment tip geometry of sheet intrusions, I: Theory and numerical models for the role of tip shape in controlling propagation pathways.

Authors: R.J. Walker[1], T.L. Stephens[1], C. Greenfield[1], S.P.A. Gill[2], D. Healy[3], S. Poppe[4]*

Affiliations: [1]University of Leicester, School of Geography, Geology, and the Environment, University Road, Leicester, LE1 7RH, UK. [2]University of Leicester, Department of Engineering, University Road, Leicester, LE1 7RH, UK. [3]School of Geosciences, King's College, University of Aberdeen, Aberdeen, AB24 3UE, UK. [4]Laboratoire G-Time, Department of Geosciences, the Environment and Society, Université Libre de Bruxelles, Brussels, Belgium.

Corresponding author: rich.walker@le.ac.uk
Corresponding author twitter handle: @DrRJWalker

Segment tip geometry of sheet intrusions, I: Theory and numerical models for the role of tip shape in controlling propagation pathways.

R.J. Walker[1*], T.L. Stephens[1], C. Greenfield[1], S.P.A. Gill[2], D. Healy[3], S. Poppe[4]
[1]University of Leicester, School of Geography, Geology, and the Environment, University Road, Leicester, LE1 7RH, UK.
[2]University of Leicester, Department of Engineering, University Road, Leicester, LE1 7RH, UK.
[3]School of Geosciences, King's College, University of Aberdeen, Aberdeen, AB24 3UE, UK.
[4]Laboratoire G-Time, Department of Geosciences, the Environment and Society, Université Libre de Bruxelles, Brussels, Belgium.

*Corresponding author: rich.walker@le.ac.uk

ABSTRACT

Inferences about sheet intrusion emplacement mechanisms have been built largely on field observations of intrusion tip zones: magmatic systems that did not grow beyond their observed state. Here we use finite element simulation of elliptical to superelliptical crack tips, representing observed natural sill segments, to show the effect of sill tip shape in controlling local stress concentrations, and the potential propagation pathways. Stress concentration magnitude and distribution is strongly affected by the position and magnitude of maximum tip curvature κ_{max}. Elliptical tips concentrate stress in-plane with the sill, promoting coplanar growth. Superelliptical tips concentrate maximum tensile stress (σ_{max}) and shear stress out-of-plane of the sill, which may promote non-coplanar growth, vertical thickening, or coplanar viscous indentation. We find that $\sigma_{max} = A\sqrt{\kappa_{max}}$, where A is a constant. At short length-scales, blunted tips have locally large σ_{max}; at longer length-scales, elliptical-tipped sills become more efficient at concentrating stress than blunt sills.

PLAIN LANGUAGE ABSTRACT

Magma sheets underground grow in stages: small isolated sheets grow, link, and inflate to become larger/longer sheets. Preserved tips at the ends of sheets are inferred to represent these growth stages. However, a number of processes may alter the shape of sheet tips, which operate after growth. Here we model idealised shapes representing natural sheet tips, to determine the efficiency of those shapes – how likely they are to facilitate growth – and the likely pathway for growth based on the greatest efficiency. We find that growth efficiency and direction is linked to the magnitude and position of the maximum tip curvature. Elliptical tips have one maximum curvature at the tip, and will promote continued growth along the long axis of the sheet: small sheets will grow to become longer sheets. Squared-ellipses can be efficient, but a single tip displays two maximum curvature zones, which may change the growth pathway.

1 INTRODUCTION

Igneous sheet intrusions are a fundamental component of volcanic plumbing systems, representing conduits that supply volcanic eruptions, nascent magma storage systems in the crust, and fundamental building blocks of oceanic (Gass, 1968; Maclennan, 2019) and continental crust (Jackson et al., 2018). Sheet intrusions that grow close to Earth's surface can induce large earthquakes and surface ruptures, in some cases leading to volcanic eruption (Wright et al., 2012; Sigmundsson et al., 2015). The distribution of earthquakes during intrusion, and the nature of surface deformations (e.g., doming, graben formation, and fissuring) is proposed to be related to the shape of the intrusion and the stages of its growth: the style and magnitude of surface deformations relate to the length, thickness, and tip geometry of the magma sheet (Mastin and Pollard, 1988; Rubin and Pollard, 1988).

Magma sheet growth models and emplacement mechanisms are critical to contemporary studies of active intrusions, since they provide key insights into the signatures of seismicity during active magma sheet growth (Pallister et al., 2010), the role of magma sheets in volcano flank instability (McGuire, 1996), and surface topographic effects of intrusion in planetary rift systems (Rubin, 1992; Wilson and Head, 2002; Wyrick and Smart, 2009). A number of models have been proposed for sheet intrusion propagation (Rivalta et al., 2015; Galland et al., 2018; Stephens et al., *in review*), including: (1) the splitting model (Lister, 1990; Rubin, 1993), related to tensile stress concentration at the tip according to linear elastic fracture mechanics (LEFM) (e.g., Fig. 1); (2) the LEFM-Barenblatt cohesive zone model

(Rubin, 1993); (3) host rock shear-failure models, via brittle and/or ductile tip zone faulting (Pollard et al., 1973), or viscous indentation (Merle and Donnadieu, 2000; Spacapan et al., 2017) (e.g., Fig. 2G); and (4) host rock fluidization (Schofield et al., 2010) (e.g., Fig. 2C). These models are founded largely in field observations of natural intrusions; however, it is not possible to directly observe the growth of sheet intrusions.

Several recent laboratory and numerical models, coupled to field observations of intrusions in relatively weak host rocks (e.g., mudstones: Schmiedel et al., 2017; Haug et al., 2018; Poppe et al., 2019; Souche et al., 2019) have highlighted the role of host rock material properties in controlling the intrusion emplacement mechanism. Sill emplacement in mudstones can be accommodated through host rock shear failure (Haug et al., 2017; Galland et al., 2019). Shear failure typically associates with blunted finger-like intrusion geometries, rather than the classical bladed shapes (e.g., Fig. 1) that have formed the basis for propagating models using a LEFM framework for the past 50 years (e.g., Pollard 1973; Mastin and Pollard, 1988; Gudmundsson, 2002; Magee et al., 2019).

The purpose of the present two-part contribution (see Stephens et al., *in review*) is: (1) to demonstrate the effects of sill tip geometry on propagation potential, using Finite Element (FE) models, for a range of idealised non-bladed tip shapes (e.g., Fig. 2); (2) to critically assess the inference that intrusion segments represent the early stages of the intrusion process; and (3) to propose an evolutionary model for intrusion emplacement (Stephens et al., *in review*).

2 Background: Relating crack shape to stress in the host rock

Emplacement of sheet intrusions has been widely considered to occur in stages, with (1) initial fracture propagation, followed by (2) magma flow through the fracture, and (3) fracture inflation by magma pressure inside the fracture (Baer, 1995). Initial fractures are segmented, and may exhibit minor offsets in the position of fracture planes; their propagation leads to interaction and linkage, which preserves these offsets, as steps in the sheet wall, or remnant and abandoned tips (e.g., Figs. 1 and 2; Pollard et al., 1975; Francis, 1982; Rickwood, 1990). Preserved tips and isolated segments are therefore treated as being representative of the growth stages of sheet development (Magee et al., 2019). This classical model for sheet emplacement has been generally considered as an elastic-brittle process, in which magma pressure in the intrusion performs work on the intrusion walls in a hydraulic fracture (Rubin, 1995; Gill and Walker, 2020). Deformation ahead of the tip occurs as elastic bending of the host rock to accommodate the gradual gradient of the intrusion thickness (Fig. 1). The intrusion fracture will grow when the tip stress intensity factor K equals the material fracture toughness K_c. For a non-growing crack subjected to a uniform internal pressure ΔP,

$$K = \Delta P\sqrt{a}, \qquad (1)$$

where a is the major semi-axis of the crack (Rubin, 1995). If the crack is growing, Equation 1 must be expanded to account for a spatially variable excess pressure (Lister and Kerr, 1991). The $K = K_c$ fracture criterion is commonly applied in the sheet intrusion literature because dykes and sills have generally been treated as a Linear Elastic Fracture Mechanics (LEFM) problem. The only geometric term considered is the crack length, since the assumption is that the crack is sharp; hence K does not directly apply to non-bladed (i.e. blunt) cracks.

Crack shape has long been considered in terms of stress concentration with respect to tensile loading (note that, here we reckon tensile stress positive and compressive stress negative, such that the maximum tensile stress is σ_1 and the least tensile stress is σ_3; Pollard and Fletcher, 2005) of an infinite elastic medium containing an elliptical hole (Kirsch, 1898; Inglis, 1913; Eshelby, 1957), where the local maximum tensile stress at the tip due to an applied remote stress is

$$\sigma_{max} = \sigma_\infty(1 + 2\frac{a}{b}), \qquad (2)$$

where a and b are respectively the major and minor semi-axes of the hole, and σ_∞ is the applied remote tensile stress at distance from the hole, applied parallel to b (Inglis, 1913). This reduces to $\sigma_{max} = 3\sigma_\infty$ in the case of a circular hole ($a = b$), whereas for cracks, $b \to 0$ hence σ_{max} should theoretically increase towards infinity at the crack tip. Since materials cannot withstand infinite stress, the stress concentration is capped by non-elastic deformation in the tip region, which is commonly referred to as the *process zone*. We can define tip radius of curvature for an elliptical crack as $\rho = \frac{b^2}{a}$, hence the tip zone stress concentration related to externally-applied loads for elliptical cracks becomes

$$\sigma_{max} = \sigma_\infty(1 + 2\sqrt{\frac{a}{\rho}}). \qquad (3)$$

Several studies of intrusion tip segment shapes, particularly on the lateral periphery of igneous sills, have shown that segments can exhibit relatively blunted forms (e.g., Fig. 2), with superelliptical (i.e., Lamé curves, Lamé, 1818) cross sections in the tip region (compare Figs. 1 and 2). The superellipse curve form can be defined by

$$\left(\frac{x}{a}\right)^n + \left(\frac{y}{b}\right)^n = 1, \qquad (4)$$

where $n = 2$ will give a circle if $a = b$, or an ellipse if $a > b$ (Figs. 2 and 3). Superellipses have geometries ranging from a cross ($n \to 0$) to a square/rectangle ($n \to \infty$, e.g., Figs. 2 and 3). Superellipse geometries where $n > 2$ do not exhibit a single tip maximum curvature κ_{max} (where $\kappa_{max} = \frac{1}{\rho_{min}}$; see Fig. 3B), nor a simple relationship between the axis length-scales and tip curvature. Superellipses therefore pose issues for calculation of stress intensity K, and there are few analytical solutions for the stress around superelliptical tips (see e.g., Greenspan, 1944; Obert and Duvall, 1967). Solutions for stress concentration around superelliptical cracks subjected to an external load (e.g., Greenspan, 1944) show that tip form affects the magnitude and distribution of σ_{max} around the tip, with increasingly superelliptical tips (i.e., higher n) moving σ_{max} increasingly out of plane of the crack. Here we apply this principle to consider the effect of superelliptical tips in controlling the magnitude and distribution of σ_{max} for fluid pressure internal to a crack, and therefore the potential pathways of intrusion growth.

3 METHODS

To consider the effects of superelliptical tip geometries on the stress induced in the surrounding host rock, we present 2-D linear-elastic models for a range of sill tip shapes, including elliptical and superelliptical (Figs. 2 and 3) curves. The models can be applied to dykes by rotating the reference frame by 90°, but here we will consider horizontal intrusions. The models are constructed using the finite element (FE) software COMSOL Multiphysics (v5.5). Intrusion tip geometry variation is a consequence of some combination of material and environmental conditions and the resulting dominant deformation processes, and can be modified by non-elastic processes (Rubin, 1995) such as: (1) mechanical and/or thermal erosion (Delaney and Pollard, 1981; Bruce and Huppert, 1990); (2) distributed faulting (Rubin, 1992); and (3) syn- and post-intrusion viscous deformations in the host rock (Rubin, 1993; Schmiedel et al., 2017). Here, we prescribe a static sill geometry within a linear-elastic medium, and apply a constant magma pressure $P_m = 1\ MPa$ internal to the sill. To isolate the effect of sill tip geometry, we do not apply any other stress state to the material volume (i.e. the host rock lithostatic pressure $P_L = 0MPa$); the stress perturbation in the host rock is solely the result of excess pressure P_e ($= Pm$ in this case) within the crack.

The 2-D model space comprises an isotropic and homogenous elastic medium. The model space is sufficiently large to avoid stress interaction with the boundary: In all models, the sill major semi-axis a is 15% of the x dimension of the model space, and stress is zero at the model extremities. Figure 3 shows the model symmetry axes. Material and model parameters are chosen to avoid significant strain within the material for the applied magnitude of P_m. The host rock has a Poisson's ratio $\nu = 0.25$, and Young's modulus $E = 40\ GPa$, though since these are linear elastic models, these properties only affect the scale of distribution of stress amplification: larger ν and/or smaller E would amplify the effect of an applied stress. As noted above, the pressure applied within the sill represents an excess pressure $P_e = P_m - P_L$. The magma pressure serves as a reference pressure to which all other stress is relative, and changes in the applied stress would result in a linear change in resolved stresses within the host rock. Stresses in FE simulation are dependent on the model size and the mesh size. As a consequence of the finite model size, and the mesh size, the infinite stress predicted for a bladed crack is reduced to a finite value. As noted above, this limit would be imposed by non-elastic deformation within the process zone ahead of the tip.

Modelled sill dimensions are varied to consider (a) the effect of tip shape on the magnitude and distribution of stress in the host rock, and (b) the relative effect of tip shapes for sills of different lengths as a function of sill aspect ratio $R = \frac{a}{b}$. Tip shape is varied within the models by changing the n exponent in Equation 4, in the range 2 to 100, and we consider each sill tip shape for a range of aspect ratios $R = \{2, 5, 10, 50, 100, 1000\}$. For an ellipse –a superellipse where $n = 2$, which separates cross-like superellipses ($n < 2$) from squared-appearance superellipses ($n > 2$) – the curvature is given by:

$$\kappa = \frac{1}{a^2 b^2}\left(\frac{x^2}{a^4} + \frac{y^2}{b^4}\right)^{-\frac{3}{2}}. \qquad (5)$$

As noted above, the minimum radius of curvature for an ellipse is given by $\rho_{min} = \frac{b^2}{a}$, and $\kappa_{max} = 1/\rho_{min}$. The relationship for a superellipse where $n > 2$ is more complex, as κ_{max} splits to a position above and below the centre-line of the crack. In Cartesian form, the curvature of a superellipse is

$$\kappa = -\frac{(n-1)x^{n-2}y^{n-2}}{a^n b^n \left(\frac{x^{2n-2}}{a^{2n}} + \frac{y^{2n-2}}{b^{2n}}\right)^{3/2}}. \quad (6)$$

The parametric form for a superellipse is $x = a\cos^m\theta$ and $y = b\sin^m\theta$, where $m = \frac{2}{n}$, and the curvature κ is given by

$$\kappa(\theta) = \frac{x'y'' - y'x''}{(x'^2 + y'^2)^{\frac{3}{2}}}, \quad (7)$$

where $x' = dx/d\theta$ etc. Hence, we can write

$$\kappa(\theta) = \frac{\eta(2-m)}{am} f(\theta, \eta) \quad (8)$$

where $\eta = \frac{b}{a} = \frac{1}{R}$ and

$$f(\theta, \eta) = \frac{\sin^{m-4}\theta \cos^{m-4}\theta}{(\cos^{2m-4}\theta + \eta^2 \sin^{2m-4}\theta)^{\frac{3}{2}}}. \quad (9)$$

This is minimised when

$$\eta^2 = \frac{(m-4) + 2(m-1)\tan^2\theta}{\tan^{2m-4}\theta[2(m-1) + (m-4)\tan^2\theta]}. \quad (10)$$

This is a non-linear function in $tan\theta$ so there is no analytical solution. We solve by calculating $\eta^2(\theta)$ and then given the value of η^2 interpolate the function to find the critical value of θ (see Supplementary files). We validate calculated κ_{max} by plotting the superellipse curve and taking the curvature as a step function, which we perform in MATLAB. This method, and resulting value for κ_{max}, is limited as it is dependent on the step size, and for superellipses with large n, the step size must become vanishingly small. Comparison of results for κ_{max} based on Equation 6 in the range of n and R where step-size is not a limitation, and results from Equations 7-10 are in agreement to three decimal places, which is more than sufficient for our purposes. Figure 3C shows the results of calculated maximum curvature as a function of n for a range of aspect ratios (1-1000).

4 Results and Interpretation

Propagation of a sill through our modelled isotropic host medium would be most likely where the tensile stress and/or the shear stress concentration is at its maximum (i.e., σ_{max} and/or τ_{max}), and is therefore most likely to exceed the host rock strength. The mode of failure (extension, extensional-shear, or compressional-shear) is controlled by the conditions of stress at the tip, though it should be noted that our models describe the approach to failure, and not the failure itself. Increasing the aspect ratio of modelled elliptical sills ($n = 2$) from $R = 1$ to $R = 1000$ causes an increase in the stress concentration at the position of maximum curvature κ_{max}, at $\theta = 0°$, as is expected from Equations 1 and 3 (Figs. 4 and 5): we find that $\sigma_{max} = A\sqrt{\kappa_{max}}$, where A is a constant (Fig. 5E). Inspection of Figure 5D suggests that deviation from the power law trend at the upper extremity of the regression is a mesh size-related underestimation of stress for the very sharp tip region of the $R = 1000$ ellipse.

Changing the tip region shape to superelliptical geometries, as a function of the n exponent, results in two key changes to stress concentrations in the host rock: (1) changes to the maximum stress generated; and (2) changes to the position of that maximum stress with respect to the horizontal centre line of the sill (Figs. 4 and 5). For superellipses with aspect ratio $R = 2$, increasing n from 2 (elliptical) to 3 (a slightly-squared ellipse; e.g., Fig. 3B) results in a decrease in resolved tensile stress in the host rock (Fig. 5A-B). Increasing n from 3 to 100 (a rectangle at the scale of observation; e.g., Fig. 3B) results in a significant increase in the maximum stress generated in the host rock, such that

where $n \geq 5$, σ_{max} is larger than that recorded for an elliptical intrusion of the same aspect ratio (Figs. 5A-B); σ_{max} for an ellipse is ~19% of the magnitude recorded for a superellipse where $n = 100$ (Fig. 5B).

Increasing superellipse aspect ratio results in a relatively diminished effect of increasing n, such that where $R \geq 50$, an ellipse ($n = 2$) records a larger stress concentration than superellipses in the study range and at the same aspect ratio (Fig. 5A-B). The relative effect of sill aspect ratio on stress concentration as a function of n is highlighted by normalizing stress concentrations relative to those recorded for $R = 2$ (Fig. 5D). We attribute this to the change in maximum curvature, which is a function of the sill aspect ratio and the tip shape (Fig. 5E). Increasing the aspect ratio of an ellipse results in an increase in the maximum curvature by about six orders of magnitude from $R = 2$ to $R = 1000$ (Figs. 3C and 5E). Superellipses where $R = 2$ and $n \to 100$, already have a large κ_{max} at the apparent-squared corners of the tip. At any aspect ratio, a superellipse where $n = 100$ appears indistinguishable from a rectangle at the scale of observation: Increasing the aspect ratio for large n segments (from $R = 2$ to $R = 1000$) increases the maximum curvature only by about three orders of magnitude (Fig. 3C). As with ellipses, we find that for superellipses $2 < n \leq 100$, $\sigma_{max} = A\sqrt{\kappa_{max}}$ (Fig. 5E).

Figure 4 shows that for superellipses where $n > 2$, σ_{max} and τ_{max} move increasingly out-of-plane as n increases. Figure 5C shows the position of σ_{max} in the y coordinate normalized to the half-thickness (b) of the intrusion; i.e., where $\frac{y}{b} = 0$, the maximum stress is along the sill centre axis. For elliptical sills ($n = 2$) we expect coplanar growth initiated at the site of σ_{max}, producing a longer, flat sill ($\frac{y}{b} = 0$). Increasing n moves σ_{max} progressively away from the sill centre axis ($0 < \frac{y}{b} < 1$). The non-coplanar distribution of maximum stress for superellipses may result in a number of growth scenarios, which we discuss below.

Our linear elastic models for stress distributions around static sill segments show that tip shape – here simplified to elliptical to superelliptical curve forms – is important in controlling the magnitude of stress concentration at the tip, and the position of that maximum stress. Blunted tip shapes concentrate stress out of plane of the sill, with the position of maximum stress corresponding to the position of the maximum tip curvature (Fig. 4). For small aspect ratio segments, blunted tips may be more efficient at concentrating stress than ellipses (Fig. 5B), as a consequence of the larger curvature associated locally with the squared superellipse corners. Increasing the aspect ratio of an ellipse or superellipse characterised by a small n-exponent results in a significant increase in the maximum stress, as a consequence of the increased tip zone curvature. In contrast, increasing the aspect ratio of superellipses characterised by a large n-exponent, results in a minor change to the tip curvature relative to short segments.

5 Discussion

5.1 Tip shape and stress concentration in the host rock

Segment tip-zone curvature imposes a sill-length-dependent control on the maximum stress generated in the host rock (Fig. 5), and controls the position of that maximum stress change within the host rock relative to the centre line of the sill major axis (Figs. 4 and 5). These findings have implications for (1) the growth potential of sheet intrusions, and (2) the results of other intrusion simulations and laboratory models. Recent numerical models using circular, superelliptical, or rectangular tips (Hardy, 2016; Vachon and Hieronymus, 2017; Haug et al., 2017, 2018; Souche et al., 2019) have shown that such geometries tend to be characterised by shear failure in the host rock, supporting field examples of shear-dominated viscous indentation of the host rock (e.g., Spacapan et al., 2017; Galland et al., 2019). Haug et al. (2017, 2018) found that short sills (in their case, $a = 200\,m$) of constant thickness ($b = 25\,m$), with a semi-circular tip region ($\rho_{min} = 25\,m$ and $\kappa_{max} = 0.04$), required an excess pressure of >900 MPa to cause shear failure of the host rock; longer sill segments ($a > 4\,km$) required much less magmatic overpressure (i.e., < 60 MPa). This decrease in the required excess pressure is to be expected given the relationship between stress intensity and crack length (e.g., Equation 1), since the key length scale controlling tip stress is the fracture length. Their sills were modelled at ~2 km depth, where a natural host rock *in situ* tensile strength should be expected to be on the order of 3-5 MPa, and the shear stress at failure may be <50 MPa. As noted by Haug et al. (2017), it is unreasonable to expect such large magma overpressures within a static sill, at such a depth on Earth; estimates for the likely range of possible magmatic overpressure in sills is 1-20 MPa (Rubin, 1995). Although not directly comparable, the models in Haug et al. (2017, 2018) are similar to the relatively blunted (superelliptical), tips modelled here since the tip curvature is less than it would be for an elliptical sill of the same dimensions. Using the example above ($a = 200\,m$ and $b = 25\,m$), the equivalent elliptical crack would have a maximum tip curvature $\kappa_{max} = 0.32$ as opposed to their $\kappa_{max} = 0.04$. The maximum stress is proportional to the square root of the maximum curvature, hence an elliptical sill would require significantly lower magma overpressure to grow. The chosen crack dimensions and geometry of the crack tip imposes a

control on the magnitude and distribution of stress in the host rock, and this must be taken into account when interpreting model results.

Our results indicate that blunted tip shapes ($n > 2$), which are tip-forms that require non-elastic processes within the host rock, will produce stress maxima out of plane from a sill. There are four main possibilities for continued sill growth: (1) intrusion by tensile or mixed mode failure in the host rock, at the site of κ_{max} and σ_{max} (Fig. 4A); (2) horizontal growth by viscous indentation of the host rock, activating low-angle shear planes (e.g., as shown in Figure 4C for $n = 100$); (3) roof uplift and vertical inflation of the sheet, activating steep shear planes (e.g., as shown in Figure 4C for $n = 100$); or (4) arrest of the blunted sill tip, leading to growth at some other position on the intrusion, or formation of a new sill plane. This final option could result in a large number of short intrusions that may be distributed at different levels within the host rock, and may therefore account for: (a) observed inconsistent stepping of sill segments (e.g., Schofield et al., 2012; Magee at el., 2019); (b) a large number of short sills particularly in host rocks that regularly show blunted tips (e.g., mudstones; Galland et al., 2019; Mark et al., 2019); and (c) long, finger-like segments with blunted lateral tip zones (Pollard et al., 1975; Wilson et al., 2016).

For finger-like intrusions, the terminal (growing) end of the intrusion may not necessarily match the geometry of the lateral tips. Previous constant-pressure static sill models (Haug et al., 2017, 2018) indicated that sills emplaced by shear-failure would not grow as flat coplanar sheets; paradoxically, each increment of sill growth in their models stepped out of plane, and it is therefore difficult to envisage how flat intrusive sheets might grow for long distances via a macro-scale shear-dominated failure mechanism. Large tensile and shear stresses at the blunted tip corners (Fig. 4) may facilitate opening or mixed mode host rock failure, in which case – should the magma pressure exceed the normal stress on the newly-formed plane – the intrusion would grow as an inclined sheet; at least initially.

Alternatively, viscous indentation and/or fluidisation of the host rock ahead of a blunted tip, may facilitate coplanar growth, and field observations (e.g., Fig. 2C, G; Spacapan et al., 2017) and numerical simulation (e.g., Souche et al., 2019) confirm this is a viable sill-lengthening emplacement process, at least for short distances. Growth may be promoted by slip planes emanating from the large curvature zones at the corners of blunted, superelliptical tips (Fig. 4C), however, it is not an efficient growth mechanism. Unlike elastic splitting, newly-formed fault surfaces would remain in contact, and slip would be subject to residual friction on the interface. Again, if magma enters the slip planes to part the surfaces, growth may become more efficient. Most natural examples of sills do not preserve magmatic injection into such slip planes; they are compressional-shear faults, and again it is difficult to envisage this emplacement mechanism operating as a long-lived process for all but very weak rocks (e.g., mudstones: Souche et al., 2019).

As will be demonstrated by Stephens et al., (*in review*) in part II, we would suggest instead that evolving conditions at the tip, including changes to the host rock and magma properties, would lead to an evolution of the dominant emplacement mechanism as the intrusion grows and arrests.

5.2 The field record of igneous sheet intrusions

Intrusion segments are generally treated as representing the staged growth of through-going sheets, with isolated segments inferred to represent the earliest stages of the process (Delaney and Pollard, 1981; Baer and Reches, 1987; Rickwood, 1990; Schofield et al., 2012), before linkage to create the sheet-like form of sills, dykes, or inclined sheets. Field-based observations of intrusive segment tips tend to be the lateral edges of the segments as viewed in the axis of bulk magma transport (e.g., Galland et al., 2019), rather than the terminal end tip region at the distal extremities of the segment (e.g., Poppe et al., 2020). In either case, observations of segment tips are of a system that did not grow further than the observed state, and therefore represent the arresting form of segments, rather than the growing form. This is important for interpretation, since the features associated with the preserved segments are biased towards processes that led to an end of growth for that particular observed segment; field-observation-based interpretations of growth processes are subject to preservation bias. We explore this point in more detail in part II, using field-based observations (Stephens et al., *in review*).

To consider the growth stages of intrusions, it is critical to identify and separate early-stage processes from features associated with late stage modification, in the conduit (Wadsworth et al., 2015; Walker et al., 2017), and in the host rock (Delaney and Pollard, 1981; Bruce and Huppert, 1990; Rubin, 1993; Bons et al., 2004; Wilson et al., 2016). As magma solidifies it undergoes physical properties alteration, particularly in terms of an increase in viscosity. Reduction in temperature, increases in crystal proportion, and/or exsolution of volatiles may each increase viscosity (Lejeune and Richet, 1995; Hess and Dingwell, 1996; Ishibashi and Sato, 2007), increasing viscous dissipation and potentially slowing magma flow to the fracture tip. At the same time, intrusion growth may lead to changes in host rock cohesive strength. For instance, a reduction in host rock cohesion may arise from pore fluid boiling, causing

distributed rock fracture (Schofield et al., 2010). Fractured rock cannot withstand elevated tensile stresses, and may instead deform by distributed slip and/or granular flow, leading to a relative blunting of the tip zone. These processes may be more prevalent in areas of the host rock that have sufficient contact time with the magma so as to allow conductive heat transfer, such as at the lateral edges of a sill, and in rocks with sufficiently low permeability as to allow pore fluid pressure to increase (e.g., mudstones). Lateral-edge tip zones, rather than frontal tip zones, are probably more commonly found in natural dyke and sill networks, and may have experienced long-lived heat transfer as magma flowed along the conduit to a frontal propagating tip region. In each of these cases, the final stages of intrusion could contribute to a change in the material properties relative to the growth stages of intrusion; those early stages of growth would be overprinted by the final stage of emplacement, leading to a bias in preserved emplacement mechanisms.

6 Conclusions

Crack tip geometry imposes a critical control on the magnitude and distribution of stress concentration ahead of a pressurized crack; a principle that we apply here to igneous sheet intrusions. Elliptical tip zones concentrate stress in-plane with the sheet and therefore growth should continue as a flat plane. Superelliptical ('blunt') tip zones concentrate stress out of plane, which may lead to (a) inclined growth with respect to the sheet plane, (b) coplanar growth via shear in the host rock, or (c) thickening of an arrested sheet.

Author Contributions

RW, TL, and DH formulated the research concept and contributed field data and examples. CG, SG, and RW developed, tested, and processed numerical models and results. SP contributed to discussion topics and field examples. All authors have contributed to the theoretical background, interpretation, and discussion.

Acknowledgements

This study was conducted without allocated funding. Catherine Greenfield is a Daphne Jackson Trust Research Fellow funded by NERC and the University of Leicester. Simon Gill is supported by a Royal Society Apex Award. Sam Poppe is supported by a frs-FNRS postdoctoral fellowship. The authors thank Tim Davis and Steffi Burchardt for discussions that benefitted the formulation of this paper.

References

Baer, G., 1995. Fracture propagation and magma flow in segmented dykes: Field evidence and fabric analyses, Makhtesh Ramon, Israel. *Physics and chemistry of dykes. Balkema, Rotterdam*, *125*, p.140.

Baer, G. and Reches, Z.E., 1987. Flow patterns of magma in dikes, Makhtesh Ramon, Israel. *Geology*, *15*(6), pp.569-572.

Bons, P.D., Druguet, E., Hamann, I., Carreras, J. and Passchier, C.W., 2004. Apparent boudinage in dykes. *Journal of Structural Geology*, *26*(4), pp.625-636.

Bruce, P.M. and Huppert, H.E., 1990. Solidification and melting along dykes by the laminar flow of basaltic magma. *Magma transport and storage*, pp.87-101.

Delaney, P.T. and Pollard, D.D., 1981. *Deformation of host rocks and flow of magma during growth of minette dikes and breccia-bearing intrusions near Ship Rock, New Mexico* (No. 1202). USGPO,.

Eshelby, J.D., 1957. The determination of the elastic field of an ellipsoidal inclusion, and related problems. *Proceedings of the royal society of London. Series A. Mathematical and physical sciences*, *241*(1226), pp.376-396.

Francis, E.H., 1982. Magma and sediment-I Emplacement mechanism of late Carboniferous tholeiite sills in northern Britain: President's anniversary address 1981. *Journal of the Geological Society*, *139*(1), pp.1-20.

Galland, O., Bertelsen, H.S., Eide, C.H., Guldstrand, F., Haug, Ø.T., Leanza, H.A., Mair, K., Palma, O., Planke, S., Rabbel, O. and Rogers, B., 2018. Storage and transport of magma in the layered crust—Formation of sills and related flat-lying intrusions. In *Volcanic and igneous plumbing systems* (pp. 113-138). Elsevier.

Galland, O., Spacapan, J.B., Rabbel, O., Mair, K., Soto, F.G., Eiken, T., Schiuma, M. and Leanza, H.A., 2019. Structure, emplacement mechanism and magma-flow significance of igneous fingers–Implications for sill emplacement in sedimentary basins. *Journal of Structural Geology*, *124*, pp.120-135.

Gass, I.G., 1968. Is the Troodos massif of Cyprus a fragment of Mesozoic ocean floor?. *Nature*, *220*(5162), pp.39-42.

Gill, S.P.A. and Walker, R.J., 2020. The Roles of Elastic Properties, Magmatic Pressure, and Tectonic Stress in Saucer-Shaped Sill Growth. *Journal of Geophysical Research: Solid Earth*, *125*(4), p.e2019JB019041.

Greenspan, M., 1944. Effect of a small hole on the stresses in a uniformly loaded plate. *Quarterly of Applied Mathematics*, *2*(1), pp.60-71.

Gudmundsson, A., 2002. Emplacement and arrest of sheets and dykes in central volcanoes. *Journal of Volcanology and Geothermal Research*, *116*(3-4), pp.279-298.

Hardy, S., 2016. Does shallow dike intrusion and widening remain a possible mechanism for graben formation on Mars?. *Geology*, *44*(2), pp.107-110.

Haug, Ø.T., Galland, O., Souloumiac, P., Souche, A., Guldstrand, F. and Schmiedel, T., 2017. Inelastic damage as a mechanical precursor for the emplacement of saucer-shaped intrusions. *Geology*, *45*(12), pp.1099-1102.

Haug, Ø.T., Galland, O., Souloumiac, P., Souche, A., Guldstrand, F., Schmiedel, T. and Maillot, B., 2018. Shear versus tensile failure mechanisms induced by sill intrusions: Implications for emplacement of conical and saucer-shaped intrusions. *Journal of Geophysical Research: Solid Earth*, *123*(5), pp.3430-3449.

Hess, K.U. and Dingwell, D.B., 1996. Viscosities of hydrous leucogranitic melts: A non-Arrhenian model. *American Mineralogist: Journal of Earth and Planetary Materials*, *81*(9-10), pp.1297-1300.

Inglis, C.E., 1913. Stresses in a plate due to the presence of cracks and sharp corners. *Trans Inst Naval Archit*, *55*, pp.219-241.

Ishibashi, H. and Sato, H., 2007. Viscosity measurements of subliquidus magmas: Alkali olivine basalt from the Higashi-Matsuura district, Southwest Japan. *Journal of Volcanology and Geothermal Research*, *160*(3-4), pp.223-238.

Jackson, M.D., Blundy, J. and Sparks, R.S.J., 2018. Chemical differentiation, cold storage and remobilization of magma in the Earth's crust. *Nature*, *564*(7736), pp.405-409.

Kirsch, C., 1898. Die theorie der elastizitat und die bedurfnisse der festigkeitslehre. *Zeitschrift des Vereines Deutscher Ingenieure*, *42*, pp.797-807.

Lamé, G., 1818. *Examen des différentes méthodes employées pour résoudre les problèmes de géométrie*. Mme. Ve. Courcier, imprimeur-libraire.

Lejeune, A.M. and Richet, P., 1995. Rheology of crystal-bearing silicate melts: An experimental study at high viscosities. *Journal of Geophysical Research: Solid Earth*, *100*(B3), pp.4215-4229.

Lister, J.R., 1990. Buoyancy-driven fluid fracture: the effects of material toughness and of low-viscosity precursors. *Journal of Fluid Mechanics*, *210*, pp.263-280.

Lister, J.R. and Kerr, R.C., 1991. Fluid-mechanical models of crack propagation and their application to magma transport in dykes. *Journal of Geophysical Research: Solid Earth*, *96*(B6), pp.10049-10077.

Maclennan, J., 2019. Mafic tiers and transient mushes: evidence from Iceland. *Philosophical Transactions of the Royal Society A*, *377*(2139), p.20180021.

Magee, C., Muirhead, J., Schofield, N., Walker, R.J., Galland, O., Holford, S., Spacapan, J., Jackson, C.A. and McCarthy, W., 2019. Structural signatures of igneous sheet intrusion propagation. *Journal of Structural Geology*, *125*, pp.148-154.

Mark, N., Schofield, N., Gardiner, D., Holt, L., Grove, C., Watson, D., Alexander, A. and Poore, H., 2019. Overthickening of sedimentary sequences by igneous intrusions. *Journal of the Geological Society*, *176*(1), pp.46-60.

Mastin, L.G. and Pollard, D.D., 1988. Surface deformation and shallow dike intrusion processes at Inyo Craters, Long Valley, California. *Journal of Geophysical Research: Solid Earth*, *93*(B11), pp.13221-13235.

McGuire, W.J., 1996. Volcano instability: a review of contemporary themes. *Geological Society, London, Special Publications*, *110*(1), pp.1-23.

Merle, O. and Donnadieu, F., 2000. Indentation of volcanic edifices by the ascending magma. *Geological Society, London, Special Publications*, *174*(1), pp.43-53.

Obert, L. and Duvall, W.I., 1967. *Rock mechanics and the design of structures in rock* (No. BOOK). J. Wiley.

Pallister, J.S., McCausland, W.A., Jónsson, S., Lu, Z., Zahran, H.M., El Hadidy, S., Aburukbah, A., Stewart, I.C., Lundgren, P.R., White, R.A. and Moufti, M.R., 2010. Broad accommodation of rift-related extension recorded by dyke intrusion in Saudi Arabia. *Nature Geoscience*, *3*(10), pp.705-712.

Pollard, D.D., 1973. Derivation and evaluation of a mechanical model for sheet intrusions. *Tectonophysics*, *19*(3), pp.233-269.

Pollard, D.D., Muller, O.H. and Dockstader, D.R., 1975. The form and growth of fingered sheet intrusions. *Geological Society of America Bulletin*, *86*(3), pp.351-363.

Poppe, S., Holohan, E.P., Galland, O., Buls, N., Van Gompel, G., Keelson, B., Tournigand, P.Y., Brancart, J., Hollis, D., Nila, A. and Kervyn, M., 2019. An inside perspective on magma intrusion: Quantifying 3D displacement and strain in laboratory experiments by dynamic X-ray computed tomography. *Frontiers in Earth Science*, *7*, p.62.

Poppe, S., Galland, O., de Winter, N.J., Goderis, S., Claeys, P., Debaille, V., Boulvais, P. and Kervyn, M., 2020. Structural and geochemical interactions between magma and sedimentary host rock: The Hovedøya case, Oslo Rift, Norway. *Geochemistry, Geophysics, Geosystems*, *21*(3), p.e2019GC008685.

Rickwood, P.C., 1990. The anatomy of a dyke and the determination of propagation and magma flow directions. In *International dyke conference. 2* (pp. 81-100).

Rivalta, E., Taisne, B., Bunger, A.P. and Katz, R.F., 2015. A review of mechanical models of dike propagation: Schools of thought, results and future directions. *Tectonophysics*, *638*, pp.1-42.

Rubin, A.M., 1992. Dike-induced faulting and graben subsidence in volcanic rift zones. *Journal of Geophysical Research: Solid Earth*, *97*(B2), pp.1839-1858.

Rubin, A.M., 1993. Dikes vs. diapirs in viscoelastic rock. *Earth and Planetary Science Letters*, *119*(4), pp.641-659.
Rubin, A.M., 1995. Propagation of magma-filled cracks. *Annual Review of Earth and Planetary Sciences*, *23*(1), pp.287-336.
Rubin, A.M. and Pollard, D.D., 1988. Dike-induced faulting in rift zones of Iceland and Afar. *Geology*, *16*(5), pp.413-417.
Schmiedel, T., Galland, O. and Breitkreuz, C., 2017. Dynamics of sill and laccolith emplacement in the brittle crust: Role of host rock strength and deformation mode. *Journal of Geophysical Research: Solid Earth*, *122*(11), pp.8860-8871.
Schofield, N., Stevenson, C. and Reston, T., 2010. Magma fingers and host rock fluidization in the emplacement of sills. *Geology*, *38*(1), pp.63-66.
Schofield, N.J., Brown, D.J., Magee, C. and Stevenson, C.T., 2012. Sill morphology and comparison of brittle and non-brittle emplacement mechanisms. *Journal of the Geological Society*, *169*(2), pp.127-141.
Sigmundsson, F., Hooper, A., Hreinsdóttir, S., Vogfjörd, K.S., Ófeigsson, B.G., Heimisson, E.R., Dumont, S., Parks, M., Spaans, K., Gudmundsson, G.B. and Drouin, V., 2015. Segmented lateral dyke growth in a rifting event at Bárðarbunga volcanic system, Iceland. *Nature*, *517*(7533), pp.191-195.
Souche, A., Galland, O., Haug, Ø.T. and Dabrowski, M., 2019. Impact of host rock heterogeneity on failure around pressurized conduits: Implications for finger-shaped magmatic intrusions. *Tectonophysics*, *765*, pp.52-63.
Spacapan, J.B., Galland, O., Leanza, H.A. and Planke, S., 2017. Igneous sill and finger emplacement mechanism in shale-dominated formations: a field study at Cuesta del Chihuido, Neuquén Basin, Argentina. *Journal of the Geological Society*, *174*(3), pp.422-433.
Stephens, T.L., Walker, R.J., Healy, D., Bubeck, A., *in review.* Segment tip geometry of sheet intrusions, II: Field observations of tip geometries and a model for evolving emplacement mechanisms
Vachon, R. and Hieronymus, C.F., 2017. Effect of host-rock rheology on dyke shape, thickness and magma overpressure. *Geophysical Journal International*, *208*(3), pp.1414-1429.
Wadsworth, F.B., Kennedy, B.M., Branney, M.J., von Aulock, F.W., Lavallée, Y. and Menendez, A., 2015. Exhumed conduit records magma ascent and drain-back during a Strombolian eruption at Tongariro volcano, New Zealand. *Bulletin of Volcanology*, *77*(9), pp.1-10.
Walker, R.J., Branney, M.J. and Norry, M.J., 2017. Dike propagation and magma flow in a glassy rhyolite dike: A structural and kinematic analysis. *Bulletin*, *129*(5-6), pp.594-606.
Wright, T.J., Sigmundsson, F., Pagli, C., Belachew, M., Hamling, I.J., Brandsdóttir, B., Keir, D., Pedersen, R., Ayele, A., Ebinger, C. and Einarsson, P., 2012. Geophysical constraints on the dynamics of spreading centres from rifting episodes on land. *Nature Geoscience*, *5*(4), pp.242-250.
Wilson, L. and Head III, J.W., 2002. Tharsis-radial graben systems as the surface manifestation of plume-related dike intrusion complexes: Models and implications. *Journal of Geophysical Research: Planets*, *107*(E8), pp.1-1.
Wilson, P.I., McCaffrey, K.J., Wilson, R.W., Jarvis, I. and Holdsworth, R.E., 2016. Deformation structures associated with the Trachyte Mesa intrusion, Henry Mountains, Utah: Implications for sill and laccolith emplacement mechanisms. *Journal of Structural Geology*, *87*, pp.30-46.
Wyrick, D.Y. and Smart, K.J., 2009. Dike-induced deformation and Martian graben systems. *Journal of Volcanology and Geothermal Research*, *185*(1-2), pp.1-11.

FIGURES

Fig. 1. Examples of bladed sheet intrusion tip geometries. (**A**) Idealised tip form for bladed intrusions. (**B**) Basaltic dykes in granitic host rock, Asir Terrane, Saudi Arabia. (**C**) Basaltic dykes in gabbroic host rock, Black Cuillin, Isle of Skye, Scotland. (**D**) Basaltic dykes in granitic host rock, Asir Terrane, Saudi Arabia, showing multiple sharp tip regions emanating from a possible earlier-stage superelliptical tip region. (**E** and **F**) Basaltic dykes in layered calcareous mudstones, Hovedøya Island, Oslo rift, Norway. Dashed white line in (F) roughly highlights host rock elastic bending to accommodate the thickness of the dykes (after Poppe et al., 2020). (**G** and **H**) Basaltic sills in sandstone, Entrada Sandstone Formation, San Rafael Desert, Utah. Note that steps in the sill shown in (H) relate to the linkage of non-coplanar sill segments during sill growth.

Fig. 2. Examples of elliptical to superelliptical sheet intrusion tip geometries. (**A**) Idealised tip form for elliptical to superelliptical, varied as a function of the n exponent (Equation 4). (**B**) Elliptical tip ($n{\sim}2$) zones of trachyte sills in sandstones of the Entrada Formation, Trachyte Mesa (Henry Mountains), Utah. (**C** and **D**) Basaltic sills with elliptical to superelliptical tips ($n < 5$) in sandstone of the Entrada Sandstone Formation, San Rafael Desert, Utah. (**E**) Basaltic dyke with elliptical tip ($n{\sim}2$) in layered calcareous mudstones, Hovedøya Island, Oslo rift, Norway (after Poppe et al., 2020). (**F**) Basaltic dyke with superellipticl tip zone ($n{\sim}100$) in granitic host rock, Asir Terrane, Saudi Arabia. (**G**) Basaltic sill with superelliptical tip ($n > 10$) hosted in thinly-bedded mudstone-siltstone-sandstone units of the Leat Shale Formation, Neist Point, Isle of Skye, Scotland. (**H** and **I**) Sill and dyke with elliptical (H: $n{\sim}2$) and superelliptical

tip (I: $n{\sim}100$) zones, respectively, hosted in bedded and foliated metasedimentary units of the Lagan Mor Formation, Isle of Mull, Scotland.

Fig. 3. The 2D finite element model space. (**A**) Magma excess pressure P_e is applied internal to the intrusion. The left and lower roller boundaries allow elastic strains in the xy plane. Note that the portrayed model space is not to scale. See text for description of variables. Right-hand pane shows the symmetry axes; Figure 4 results show the right-half of the model. (**B**) Elliptical to superelliptical tip geometries illustrating the position of minimum curvature for examples where $a = b$ and $a = 2b$ (i.e., $R = 1$ and $R = 2$ respectively). (**C**) Maximum curvature for ellipses and superellipses as a function of n and R.

Fig. 4. Modelled stress distributions for elliptical to superelliptical tip zones where $R = 2$. (**A**) Changes in the maximum stress ($\Delta\sigma_1$), and (**B**) changes in shear stress in the xy plane ($\Delta\tau_{xy}$). Absolute values of stress are provided in Figure 5. The colour scale data range is uniform for all plots of $\Delta\sigma_1$ shown in (A), and for uniform for all plots of $\Delta\tau_{xy}$ shown in (B). Note that maximum $\Delta\sigma_1$, i.e. σ_{max}, is along the sill centre axis for $n = 2$, and splits to create two zones of maxima that are increasingly off-axis with increasing values for n. $\Delta\tau_{xy}$ shows a similar splitting with increasing n; stress maxima (σ_{max} and τ_{max}) in the modelled host rock correspond to the position of maximum curvature κ_{max}. (**C**) Potential shear (slip) planes (*cf.* Pollard, 1973) plot onto $\Delta\tau_{xy}$ for $n = 2$ and $n = 100$. Light-grey shear-couple arrows show potential slip sense for growth by vertical inflation of the sill, whereas dark-grey arrows show slip sense for horizontal growth by viscous indentation, in both cases accommodated by faulting in the host rock.

Fig. 5. The relationship between modelled stress change and tip zone curvature. (**A**) Maximum modelled tensile stress change for sills of aspect ratio ranging from 2 to 1000, with curve forms varied as a function of n. (**B**) σ_{max} normalised to the value of the maximum σ_{max} for each given aspect ratio. (**C**) The y-coordinate position of σ_{max} for each given aspect ratio, normalised to the minor semi-axis b. A value of 0.0 corresponds to the sill centre axis, and a value of 1.0 is the full thickness of the intrusion. (**D**) σ_{max} for aspect ratios of five and above, normalized to the σ_{max} values for $R = 2$. (**E**) σ_{max} versus calculated maximum curvature κ_{max} for the modelled sill dimensions. Note that increases in σ_{max} show a consistent power law relationship with increasing κ_{max}, ranging from $\kappa_{max}^{0.42}$ to $\kappa_{max}^{0.55}$.

DATA AVAILABILITY AND SUPPLEMENTARY FILES

Supporting datasets will be made available via the University of Leicester's Figshare portal, to include:
Supplement 1. Calculations and calculator for determining κ_{max} based on Equations 7 to 10.
Supplement 2. Full results for numerical models of elliptical to superelliptical tips, extracted from Comsol Multiphysics.
Supplement 3. Comsol Multiphysics model file.

Fig. 1
Width: 175 mm
Height: 148 mm

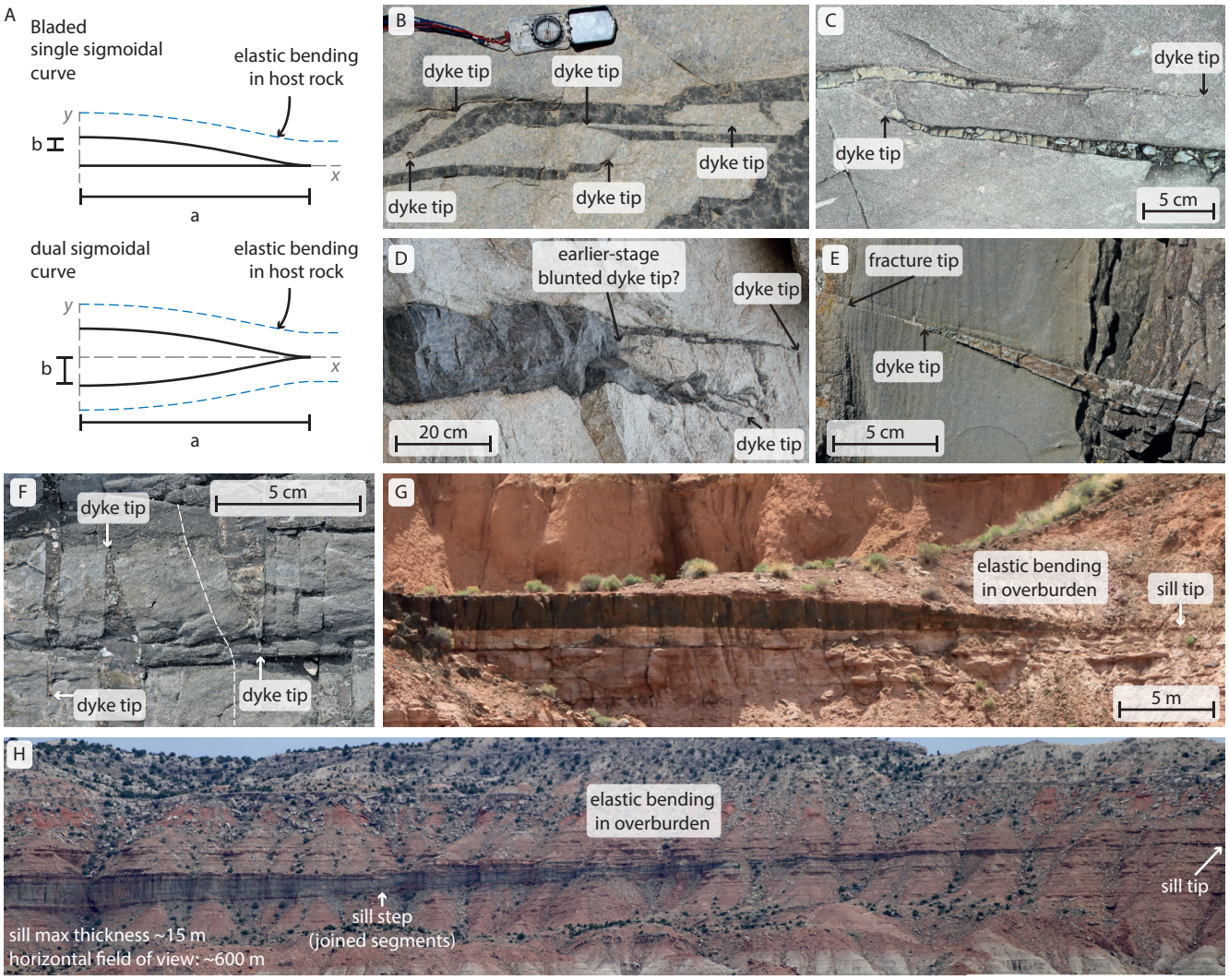

Fig. 2
Width: 175 mm
Height: 135 mm

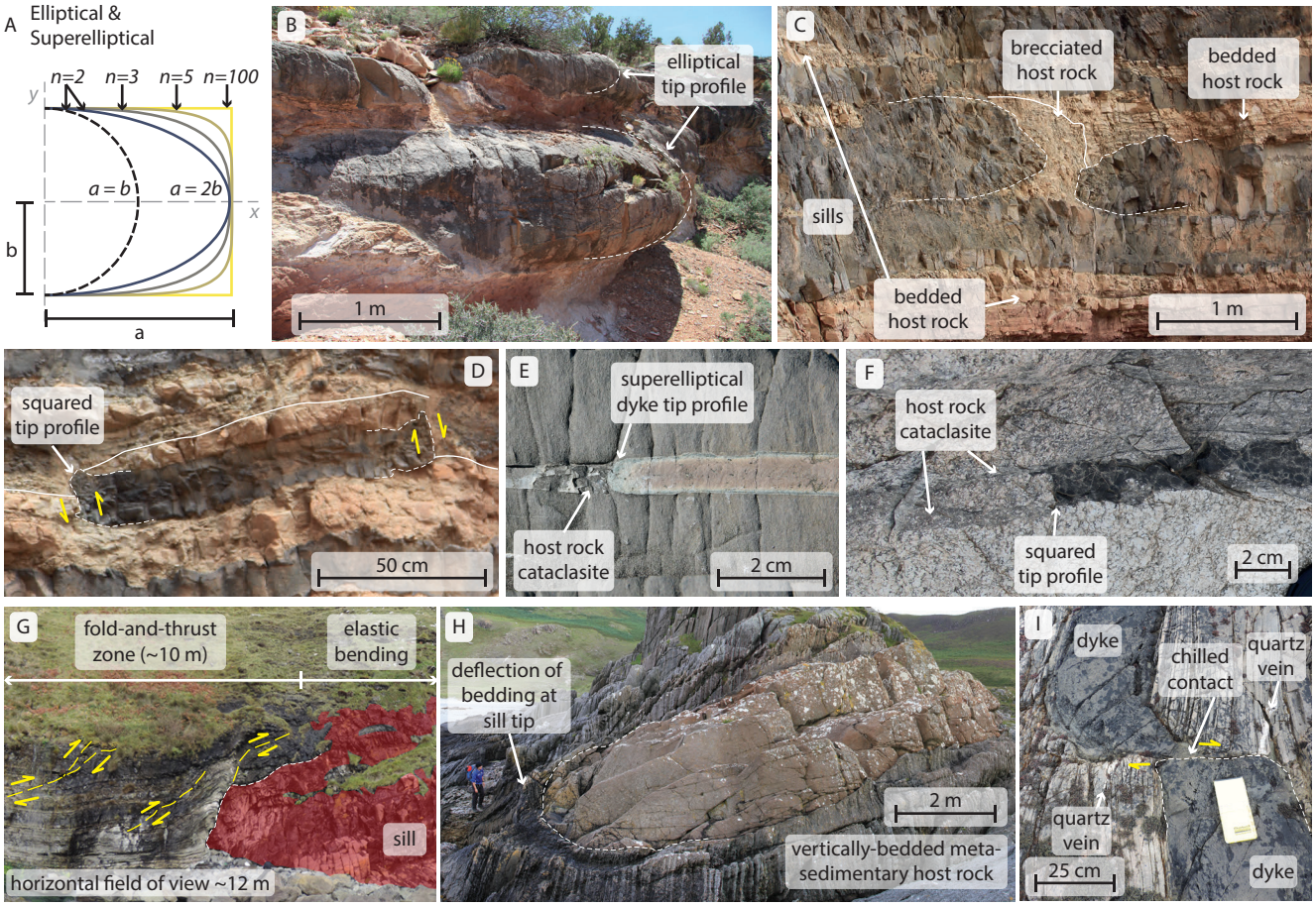

Fig. 3
Width: 175 mm
Height: 85 mm

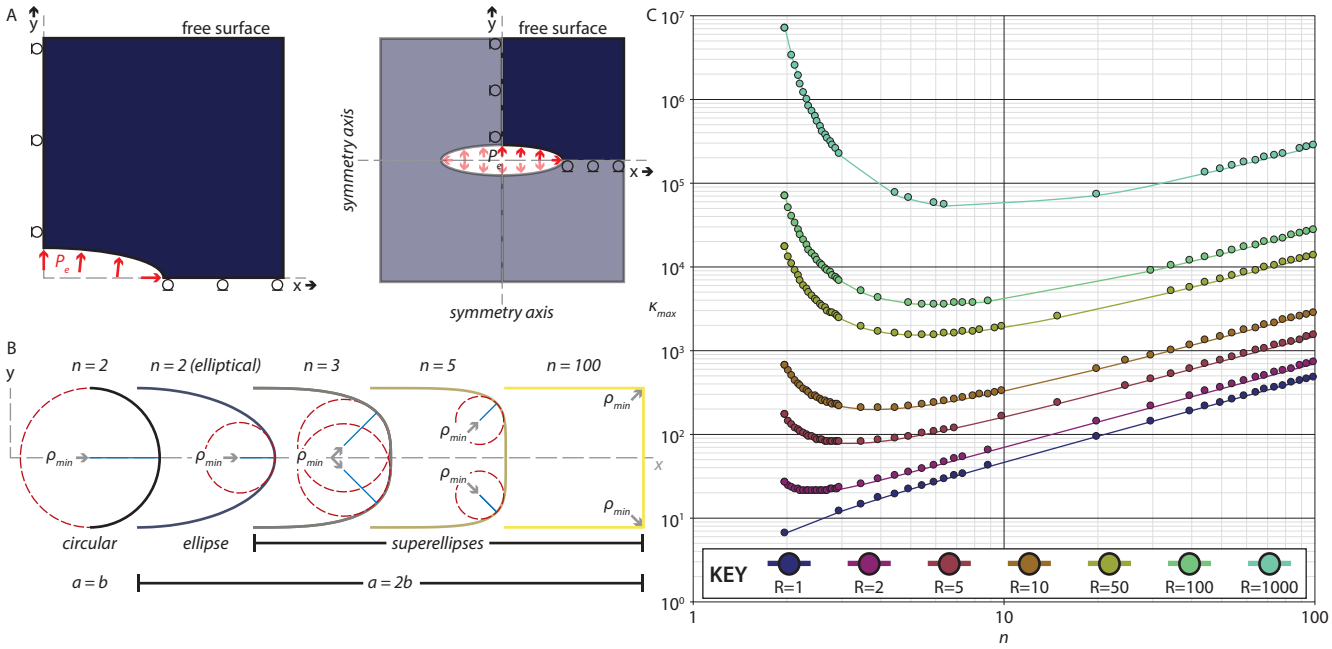

Fig. 4
Width: 175 mm
Height: 193 mm

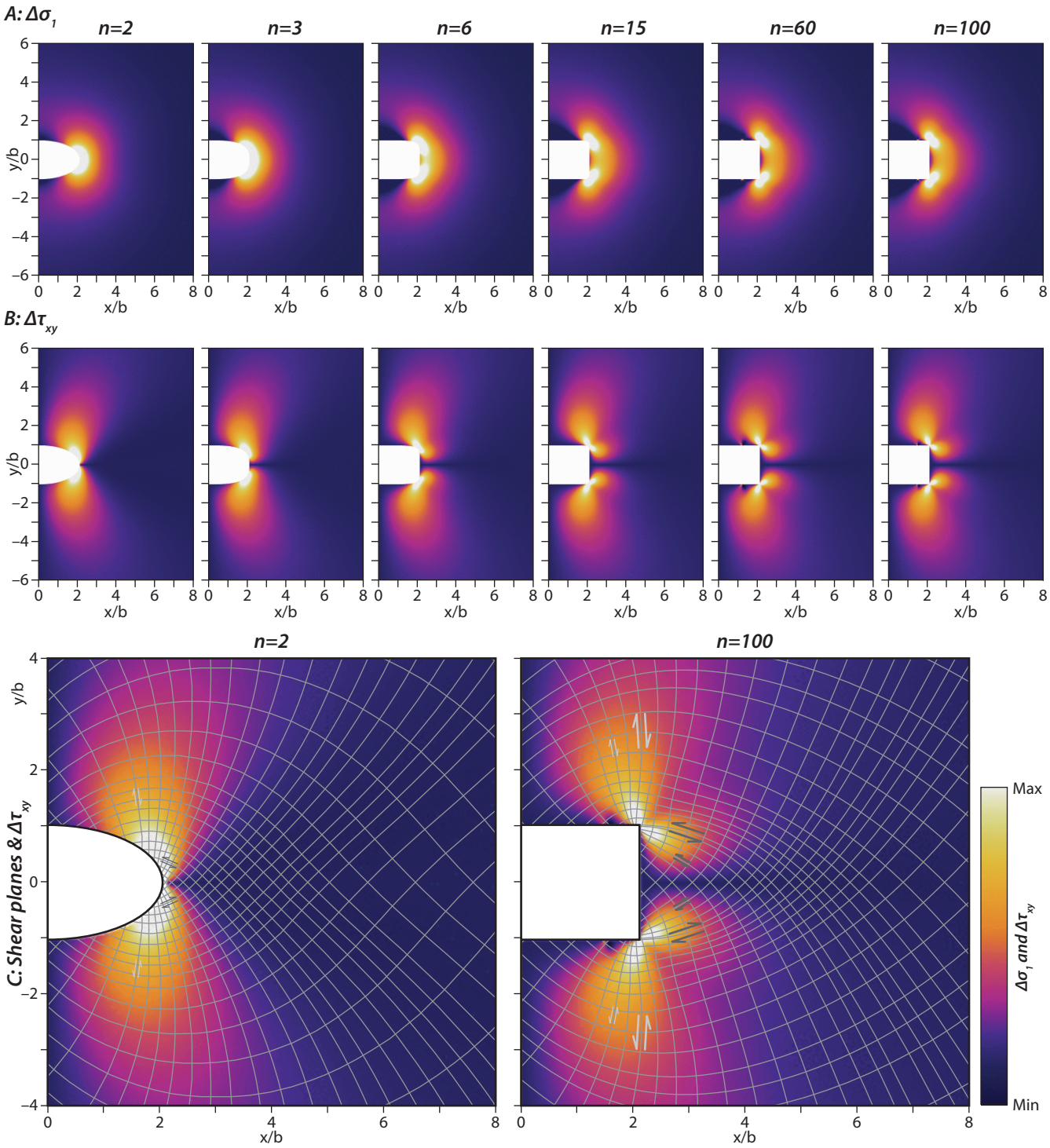

Fig. 5
Width: 175 mm
Height: 126 mm